

Nondestructive Optical Determination of Fiber Organization in Intact Myocardial Wall

REBECCA M. SMITH,^{1†} ARVYDAS MATIUKAS,^{1,2†} CHRISTIAN W. ZEMLIN,¹ AND ARKADY M. PERTSOV^{1*}

¹Department of Pharmacology, SUNY Upstate Medical University, Syracuse, New York 13210

²Department of Physics, Kaunas University of Technology, Kaunas, Lithuania

KEY WORDS myocardial fiber organization; 3D reconstruction; optical clearing; confocal microscopy; BABB

ABSTRACT Mapping the myocardial fiber organization is important for assessing the electrical and mechanical properties of normal and diseased hearts. Current methods to determine the fiber organization have several limitations: histological sectioning mechanically distorts the tissue and is labor-intensive, while diffusion tensor imaging has low spatial resolution and requires expensive MRI scanners. Here, we utilized optical clearing, a fluorescent dye, and confocal microscopy to create three-dimensional reconstructions of the myocardial fiber organization of guinea pig and mouse hearts. We have optimized the staining and clearing procedure to allow for the nondestructive imaging of whole hearts with a thickness up to 3.5 mm. Myocardial fibers could clearly be identified at all depths in all preparations. We determined the change of fiber orientation across strips of guinea pig left ventricular wall. Our study confirms the qualitative result that there is a steady counterclockwise fiber rotation across the ventricular wall. Quantitatively, we found a total fiber rotation of $105.7 \pm 14.9^\circ$ (mean \pm standard error of the mean); this value lies within the range reported by previous studies. These results show that optical clearing, in combination with a fluorescent dye and confocal microscopy, is a practical and accurate method for determining myocardial fiber organization. *Microsc. Res. Tech.* 00:000–000, 2008. © 2008 Wiley-Liss, Inc.

INTRODUCTION

The three-dimensional (3D) organization of myocardial fibers plays a crucial role in the heart's electrical and mechanical properties. It has been well documented that propagation velocities are several times faster along fibers than in the transverse direction (Panfilov and Keener, 1993; Taccardi et al., 1997), making fiber organization the most important determinant of the activation sequence (Punske et al., 2005). In addition, fiber organization is thought to play an essential role in arrhythmogenesis (Fenton and Karma, 1998; Kadiish et al., 1988); and fibers are known to be altered in some diseased states, including ischemic heart disease (Wickline et al., 1992) and ventricular hypertrophy (Koide et al., 1982; Roberts and Ferrans, 1975; Tezuka et al., 1990). Fiber organization also plays an important role in the generation of myocardial stress and strain (Omens et al., 1991; Waldman et al., 1988) and in the structural adaptation of the myocardium (Arts et al., 1994). Because fiber organization has great relevance, considerable effort has been spent to find reliable and practical methods to determine it.

The imaging tools most utilized for fiber mapping today are diffusion tensor imaging (DTI) (Burton et al., 2006; Helm et al., 2005) and histological sectioning (Vetter et al., 2005; Young et al., 1998). The main drawback of using DTI is its limited spatial resolution; only the most advanced MRI scanners can achieve a sufficient resolution ($<100 \mu\text{m}$) in a reasonable time frame ($\sim 9 \text{ h}$) (Jiang et al., 2004). Even at a resolution of $100 \mu\text{m}$, DTI is unable to identify the crossings of fiber bun-

dles adequately (Jung et al., 2006). Histological techniques provide a higher spatial resolution; however, it is difficult and labor-intensive to obtain a comprehensive 3D visualization of macroscopic specimens (Dodt et al., 2007). Sectioning the specimen may alter or destroy the normal architecture unless sophisticated schemes are used (Young et al., 1998). While confocal and two-photon microscopy avoid these limitations, they have low penetration depths of only a few hundred microns (Dodt et al., 2007).

In this article, we show how the penetration depth of confocal microscopy can be dramatically increased using optical clearing. Optical clearing is a method to make specimens transparent by matching the intra- and extracellular refractive indices and has been used in embryonic (Miller et al., 2005; Zucker et al., 1998; Zucker, 2006), tumor (Sakhalkar et al., 2007), and brain (Dodt et al., 2007) research. By adding a fluorescent dye, which binds to cell membranes, and optically clearing the heart, we were able to construct 3D renderings of the myocardial fiber organization in guinea pig and mouse hearts. We have optimized the staining

[†]R.M.S. and A.M. contributed equally to this work.

*Correspondence to: Arkady M. Pertsov, Department of Pharmacology, SUNY Upstate Medical University, 750 E. Adams St., Syracuse, NY 13210, USA. E-mail: pertsova@upstate.edu

Received 30 October 2007; accepted in revised form 9 January 2008

Contract grant sponsor: National Heart, Lung, and Blood Institute Grant; Contract grant number: 1R01-HL071635-01.

DOI 10.1002/jemt.20579

Published online in Wiley InterScience (www.interscience.wiley.com).

and clearing procedure to allow for the imaging of hearts with a thickness up to 3.5 mm.

MATERIALS AND METHODS

Preparation of Guinea Pig and Mouse Hearts for Optical Clearing

All experiments conformed to the *Guide for the Care and Use of Laboratory Animals* (NIH publication No. 85-23, revised 1996). Guinea pigs (Hartley; 300–400 g; $n = 8$) and mice (C57BL/6; 20–30 g; $n = 4$) were first heparinized (550 U/100 g for guinea pig; 250 U/20 g for mice) and then anesthetized with sodium pentobarbital (0.75 mL/100 g for guinea pig) and ketamine (200 mg/g for mice); the heart was excised and placed in ice cold cardioplegia solution (Baxter et al., 2001). The aorta was cannulated and gravity perfused with cardioplegia and diacetyl monoxime (DAM, 15 mmol/L) to inhibit contractions, and stained with either di-4-ANEPPS (5 $\mu\text{g/mL}$) or di-4-ANBDQBS (27 $\mu\text{mol/L}$) (Matiukas et al., 2007) both of which are voltage sensitive fluorescent dyes. We then dehydrated the heart by a graded ethanol series (50% (v/v), 70%, 75%, 90%, 95%, and twice in 100% for 30 min). After dehydration, the heart was treated with Murray's clear, also known as BABB (Zucker et al., 1998): 1:2 (v/v) benzyl alcohol: benzyl benzoate (both from Sigma). The time required to clear the heart was ~ 40 min. The transparent heart was stored in the clearing solution at room temperature until imaging.

Confocal Imaging and Processing

For all confocal imaging, hearts were immersed in a cuvette filled with BABB. Confocal imaging was performed on a Zeiss LSM 510 system, using a Zeiss Axiovert 200M inverted microscope with 10 \times dry and 40 \times water immersion objectives. The fluorescence was detected using 514 nm and 633 nm laser excitation and 560 nm long-pass and 650–710 nm band-pass emission filters for the dyes di-4-ANEPPS and di-4-ANBDQBS, respectively. Depth-correction of the excitation intensity and photodetector gain (z-correction function in Zeiss software) was used to reduce signal intensity variation during deep ($>500 \mu\text{m}$) scans. Repetitive scans (up to 16) were implemented to reduce the noise in the images. Whole heart scans were performed using a multiple time series software (tiled scanning with subsequent stitching of all tiles into a single image). The penetration depth for an individual scan was up to 2 mm, but we scanned specimens up to 4 mm thick by first scanning them on one side and then turning them over to image the other side. Raw images were saved as LSM files and later converted off-line to TIFF files for further processing and analysis.

Fiber Measurements

The LSM files for a particular location of the strip (base, center, or apex) were loaded into ImageJ (Abramoff et al., 2004) using the LSM toolbox plugin. The stack of slices was rotated and flipped so that the vertical axis was oriented from base to apex. The stack was band-pass filtered and the brightness and contrast was adjusted for each individual slice. The mean fiber orientation in each image was calculated using an intensity gradient algorithm as described by Karlon et al. (1998).

3D Reconstruction of Whole Heart

To create three-dimensional reconstructions of the whole heart, we first applied a median filter of radius 2 and binned the scanned data to reduce the resolution (to $\sim 100 \times 200 \times 200$ voxels). Visualization was performed using the software package Paraview (Kitware, Clifton Park, NY). We determined the signal level corresponding to the stained tissue and then computed the isosurface around the stained tissue using the Marching Cubes algorithm (Lorensen and Cline, 1987).

RESULTS

A representative photograph of a mouse heart before and after clearing is shown in Figure 1. Before clearing, light cannot pass through the heart (Panel A), while after clearing the heart is transparent (Panel B). If the heart is not immersed in BABB (Panel B), there is refractive index mismatching at the heart's surface, and the transparency is not obvious. To expose the heart's transparency, we immersed it in a cuvette filled with BABB (Panel C). In such a setting, the markings of a ruler behind the heart are clearly visible.

Figure 2 demonstrates that optical clearing dramatically improves the penetration depth of confocal microscopy. We obtained a series of optical sections of a mouse myocardium stained with di-4-ANBDQBS (Matiukas et al., 2007). In Panel A, short-axis sections start from the apex ($z = 0 \mu\text{m}$) and progress through to the base ($z = 1,680 \mu\text{m}$). At $z = 720 \mu\text{m}$, we can see the right ventricle (RV), the left ventricle (LV), and the septum, which separates the two. The papillary muscles of the LV, which protrudes from the free wall into the cavity, are seen at $z = 1,220 \mu\text{m}$. The RV can be identified by its characteristic sickle-shaped geometry; while the LV has a more cylindrical shape that appears circular in the cross-sections. Panel B shows lateral sections that start in the RV ($z = 0 \mu\text{m}$) and progress through to the LV ($z = 1,680 \mu\text{m}$). At $z = 240 \mu\text{m}$, we can see the RV and its atrium. By $z = 480 \mu\text{m}$, the septum emerges. The LV is clearly seen by $z = 1,220 \mu\text{m}$. The thickness of the ventricular walls differs substantially, with that of the right ventricular wall (1 mm) being only half that of the left ventricular wall (2 mm). Even at 1,700 μm , the signal intensity and the quality of the images are excellent; however, at larger z -values, the quality starts to deteriorate due to the residual scattering of the tissue. However, we were able to image hearts up to twice as thick (3.5 mm) by scanning first from one side and then turning the specimen over to image the other side.

Figure 3 illustrates the gross 3D anatomy reconstructed from a series of confocal sections (z-stack). In Panel A, 30 confocal slices were used to reconstruct most of the LV and part of the RV. The structure of the endocardial surface is clearly visible, most notably the papillary muscles of the LV. On the cut surface, we can see some of the gaps separating fiber bundles. Panel B shows the axial view from above of the same heart as shown in Panel A. In this panel, the myocardial tissue was darkened to make the cavities of the RV and LV more easily visible. When looking into the circular cavity of the LV, we can clearly see the 3D shape of both papillary muscles. The RV cavity has a very thin, sickle-shaped appearance (comparable with Fig. 2A).

To test whether optical sectioning can resolve individual fibers, we made strips of guinea pig right and left ventricular wall (Fig. 4). Such strips have previously been used in a variety of studies characterizing the fiber organization in different species (LeGrice et al., 1995b; Streeter et al., 1969; Vetter et al., 2005; Wu et al., 2007; Young et al., 1998). The strips were cut from base to apex, 15–20 mm in length (y-direction) and 5 mm wide (x-direction). The maximum thickness (z-direction) of the strips was ~ 2 mm for the RV and 4 mm for the LV.

Figure 5 shows that confocal sections of optically cleared tissue can clearly resolve individual myocardial fibers. We illustrate the typical fiber orientations for locations near the apex (Panel A) and the center (Panel B). Local fiber directions were computed automatically using Karlon's algorithm (Karlon et al., 1998), shown in Panels C and D. The fiber direction is highly consistent over the imaged region. To quantify fiber direction, we used a previously established notation (Vetter and McCulloch, 1998) that has the zero angle along the epicardial circumference (x-direction), positive angles oriented counterclockwise, negative angles oriented clock-

wise, and angles ranging from -90 to 90° . Using this convention, we calculated the average fiber angle for Panels A (34°) and B (-39°) as shown in Panels E and F, respectively. In this manner, we were able to quantify the fiber organization at scanning depths up to 2 mm in both RV and LV strips.

Figure 6 shows how the fiber orientation varies across the left ventricular wall. Panel A shows optical sections at the center of a guinea pig LV, which run from epi- ($z = 0 \mu\text{m}$) to endocardium ($z = 1,600 \mu\text{m}$) in steps of $200 \mu\text{m}$. Fiber orientation exhibits a gradual counterclockwise rotation with depth. To quantitatively analyze this rotation, we determined the fiber organization in six guinea pig LV preparations and computed the average orientation as a function of depth (dark solid circles, Panel B). We found that there is a steady positive rotation of fiber direction. This rotation has a biphasic nature; from 0 to 45% wall depth, the rate of rotation is 1.6° per percent depth, while from 55 to 100% depth, it is only 0.47° per percent depth. The total rotation across the ventricular wall is $105.7 \pm 14.9^\circ$ (mean \pm standard error of the mean). We compare our data to Streeter's data (light grey squares) from the center of canine LV (Fig. 5 in Streeter et al., 1969). Similar to our data, there is a continuous counterclockwise rotation with depth. However, Streeter's data have a more linear than biphasic rotation, and the total rotation is $\sim 141 \pm 10^\circ$ (mean \pm standard error of the mean), significantly more than what we observe.

Figure 7 shows a narrow guinea pig RV strip, which was cut from base to apex as described in Figure 4. Panel A shows a slice taken at $z = 60 \mu\text{m}$. The strip has been rotated for easier viewing. Fiber rotation can be easily detected everywhere from base to apex. Panel B shows fiber direction, at the location marked by the white square in Panel A, for a series of different depths, from epi- ($z = 0 \mu\text{m}$) to endocardium ($z = 620 \mu\text{m}$). These images have been rotated to match the direction of the strip in Panel A, but angles were still measured against the positive x-axis (as in Fig. 5). As for the LV (Fig. 6), there is a gradual counterclockwise rotat-

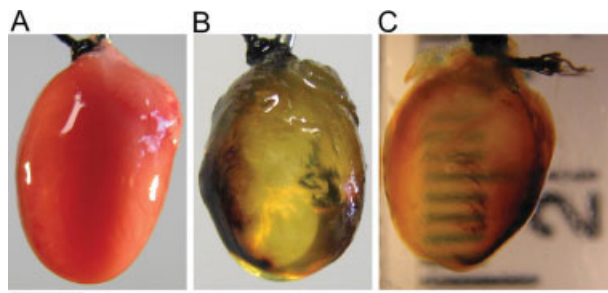


Fig. 1. Mouse heart before and after optical clearing. **A:** Mouse heart in air, before dehydration and clearing. **B:** The same heart, after dehydration and clearing with 1:2 (v/v) benzyl alcohol:benzyl benzoate (BABB). **C:** The same heart, dehydrated, cleared, and placed in a cuvette filled with BABB. A ruler was placed behind the cuvette to demonstrate the heart's transparency in BABB. Scale bar = 3 mm.

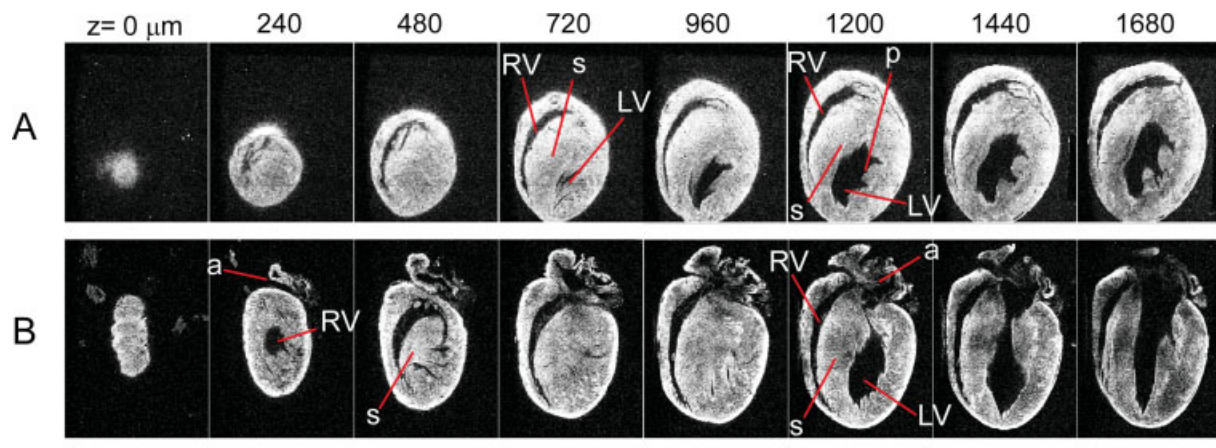


Fig. 2. Optical sections of a whole mouse heart. The heart was stained with di-4-ANBDQBS and optical sections were obtained with a $\times 10$ dry objective. **A:** Sequence of short-axis sections. Numbers on top of the panels indicate the distance from the apex. **B:** Lateral optical sections from RV to LV. Numbers above the panel indicate the distance from the RV. Landmarks indicated are LV, left ventricle; RV, right ventricle; a, atrium; s, septum; p, papillary muscle; scale bar = 5 mm.

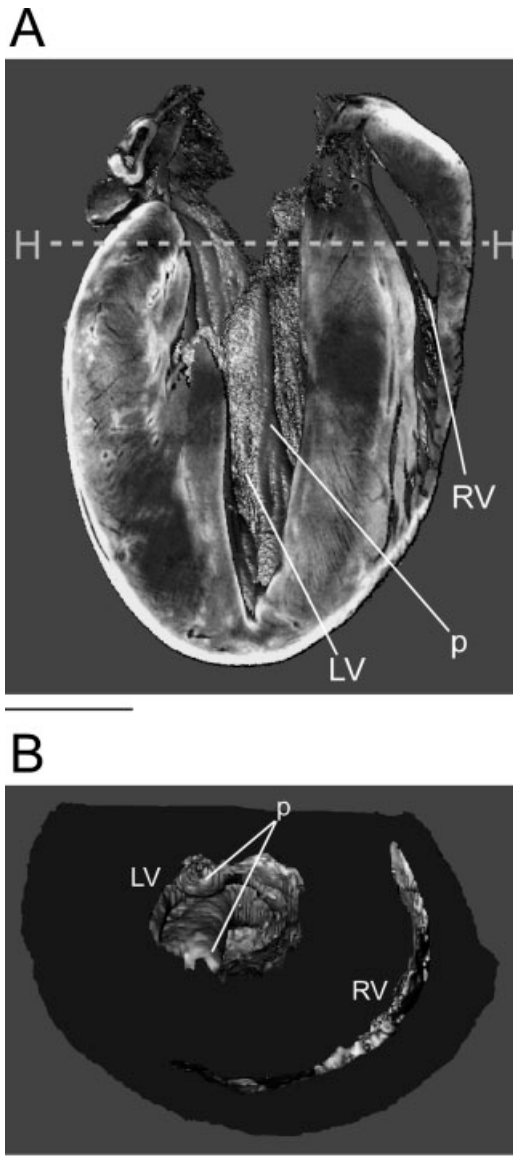


Fig. 3. Reconstructions of gross 3D anatomy from optical sections. **A:** Posterior view. We show one optical section (the cut surface) and an isosurface that encloses the 3D tissue domain. The dotted grey line is the axial (H-H) view from the heart's base at which an optical cut (B) was taken. Scale bar = 2 mm. **B:** Axial view from the heart's base. We show the cut surface (grey) and the internal surfaces of the left and right ventricles. Landmarks shown are LV, left ventricle; RV, right ventricle; p, papillary muscle; scale bar = 1 mm.

ion with respect to depth. Differently from the LV, however, there is a sigmoidal change in fiber rotation shown in Panel C. The first phase, from 0 to 50% depth, rotates at a rate of 0.75° per percent depth; a second phase of rapid rotation occurs from 55 to 65%, with a 2.8° per percent depth change. Finally, a third phase of slow fiber rotation occurs from 68 to 100% depth, with a 0.6° per percent depth change in orientation. The total rotation was $119 \pm 7^\circ$ (mean \pm standard deviation) across the ventricular wall. The graph in Panel D shows fiber direction at two depths, 60 μm (squares) and 160 μm (circles), from base to apex. The greatest differ-

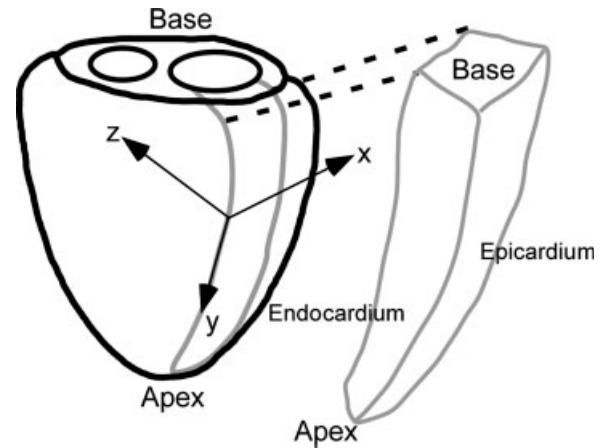


Fig. 4. Isolation of guinea pig ventricular strips to image fibers. LV (and RV) strips were cut 5 mm wide (x-direction), 15–20 mm long (y-direction), and 4 mm thick from guinea pig hearts. Similar strips were cut from guinea pig RV (thickness 2 mm).

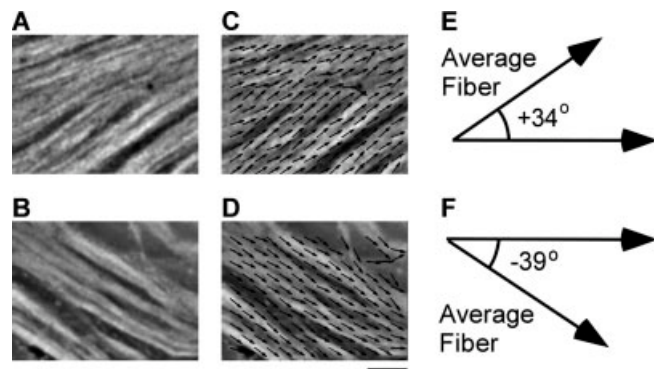


Fig. 5. Determination of fiber angle in optical sections. **A,B:** Optical sections of cardiac tissue. Scale bar = 50 μm . **C,D:** Local fiber orientations, determined with Karlson's method. **E,F:** The angle between the average local fiber orientation and the positive x-axis is the fiber angle of a given section. Counterclockwise angles (relative to the positive x-axis) are considered positive, clockwise angles negative.

ence between fiber directions at these two depths occurred at the base and apex. At the base location (y between 0 and 3.7 mm), this difference is 28° ; while at the apex location (y between 13.1 and 15 mm) it is 61° . The strong depth-dependence of fiber direction at the apex is explained by the fact that the apex is a singularity point of the fiber organization, where fibers of many different orientations meet. In the center of the strip ($4.7 \leq y \leq 12.2$ mm), fiber orientation remains fairly constant, exhibiting a rotation of about 15° within 100 μm .

DISCUSSION

The technique outlined in this article provides the framework for the qualitative and quantitative analysis of myocardial fiber orientation in 3.5 mm thick myocardium. By using optical clearing and confocal microscopy, we were able to reconstruct the 3D anatomy of the mouse heart. In addition, we were able to image myocardial fibers of 2–4 mm thick guinea pig LV and RV strips. In this manner, we have determined that

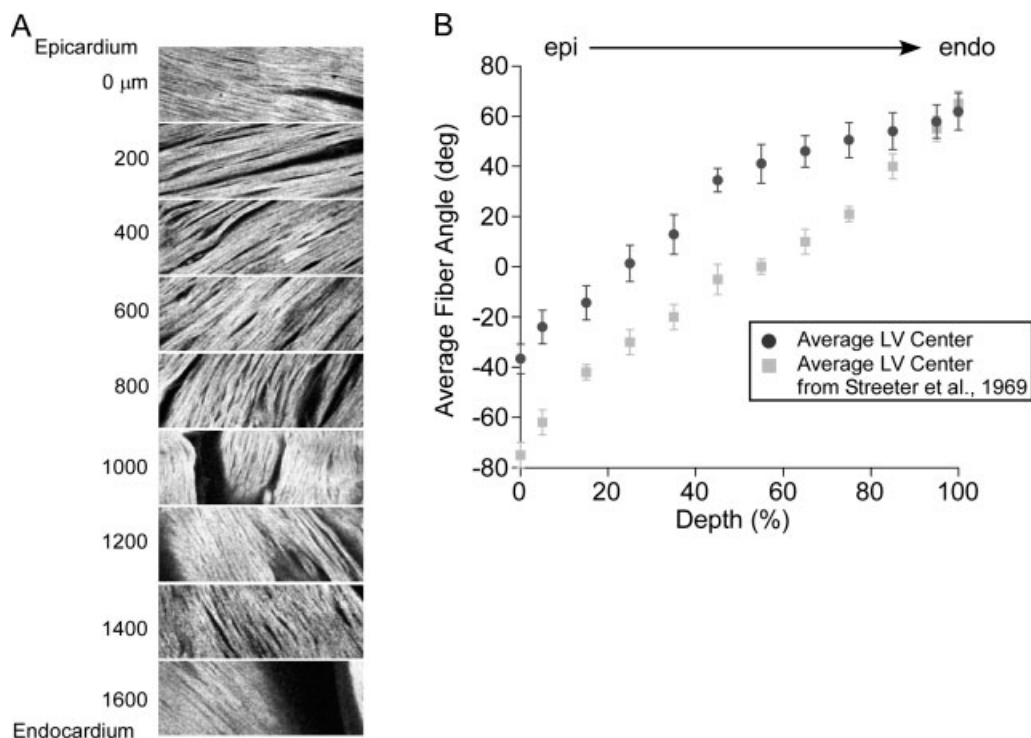


Fig. 6. Orientation of myocardial fibers in guinea pig LV. **A:** Optical sections of guinea pig LV at various depths obtained with $40\times$ water immersion objective. Numbers show the section depth starting at the epicardial surface ($0\ \mu\text{m}$). Scale bar = $50\ \mu\text{m}$. **B:** A plot of fiber angle as a function of percent wall thickness ($n = 6$, dark grey circles).

Fiber rotation in canine LV is shown for comparison (Streeter et al., 1969). Fiber angles were measured according to the notation shown in Figure 5; intramural depth is given in percent of LV wall thickness. Error bars are standard error of the mean.

there is a gradual counterclockwise rotation of myocardial fibers.

Previous studies have used DTI and histology to map myocardial fibers. DTI allows for the nondestructive mapping of myocardial fiber orientation. However, the limited spatial resolution ($<100\ \mu\text{m}$) makes it difficult to identify the crossings of fiber bundles adequately (Jiang et al., 2004). Moreover, to obtain even this spatial resolution, prolonged scan times or very powerful MRI scanners are required. DTI experiments (Holmes et al., 2000; Hsu et al., 1998; Scollan et al., 2000; Wu et al., 2007) have shown that there is a counterclockwise transmural rotation (as we observed here). Furthermore, it was determined quantitatively in canine (Hsu et al., 1998) and rabbit (Holmes et al., 2000; Scollan et al., 1998, 2000) that there is $\sim 100^\circ$ total rotation across the ventricular wall, which is in excellent agreement with our finding of $105.7 \pm 14.9^\circ$ (mean \pm standard error of the mean). However, these experiments observed a linear change in fiber rotation across the left ventricular wall as opposed to the biphasic change that we observe. This difference may be because of the different species used.

Histology has traditionally been the standard method for mapping fiber organization; it has been used to map dog (LeGrice et al., 1995a; Streeter et al., 1969), rabbit (Vetter and McCulloch, 1998), guinea pig (Hort, 1960), and rat (Omens et al., 1993; Young et al., 1998) myocardium. These experiments observed that fiber orientation has a counterclockwise rotation with

depth, consistent with both our results and those of DTI studies. However, histological studies consistently found that the total fiber rotation is significantly greater than what was reported in both DTI and our experiments. The total rotation from epi- to endocardium has been reported to be $\sim 135^\circ$ in guinea pig (Hort, 1960), 140° in dog (Hort, 1960; Streeter et al., 1969), and 180° in pig (Streeter and Bassett, 1966; Vetter and McCulloch, 1998). A possible explanation for this difference in fiber rotation lies in the procedures used in the fixation and sectioning of the specimen. In histological sectioning, formalin fixation is usually performed over a period of 18 h to 4 weeks (Holmes et al., 2000; Jiang et al., 2004; Wu et al., 2007). During fixation and subsequent dehydration of the specimen, there is substantial shrinkage (15–35%, Kanai and Salama, 1995; Streeter et al., 1969), which may cause a distortion of the fiber organization. In our proposed fiber mapping technique, preparations are not formalin fixed before dehydration in ethanol, and we observe significantly less shrinkage ($\sim 10\%$). It would be interesting to see if the total fiber rotation across the ventricular wall as determined by our method would increase if we fix our hearts before dehydration using formalin; if so, this would be important evidence that fiber mapping methods avoiding formalin fixation are more accurate. Another possible explanation for the differences between our data and that of several histological studies (Hort, 1960; Streeter et al., 1969; Young et al., 1998) is the fact that the myocardium is

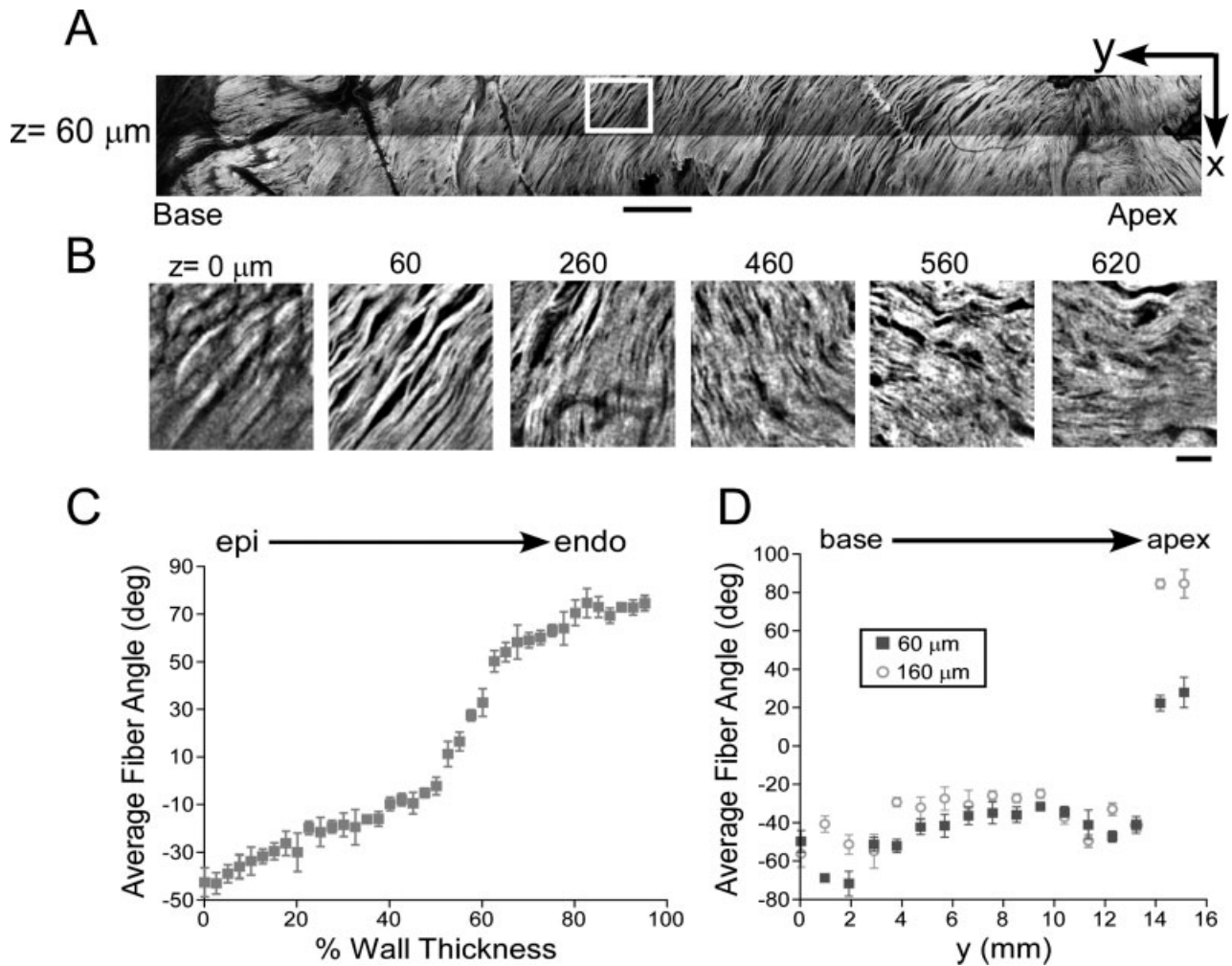


Fig. 7. Orientation of myocardial fibers in guinea pig RV. **A:** Strip of guinea pig at $z = 60 \mu\text{m}$ (from epicardial surface). The white box indicates the location that describes B, C, and D. Scale bar = 1 mm. **B:** Fiber rotation with intramural depth at the location marked by the white square in Panel A. The values indicate depth starting at the epicardial surface (0 μm). Scale bar = 50 μm . **C:** Average fiber angle

vs. intramural depth for the sections at the same location as in (B). Error bars are expressed as standard deviation. **D:** Average fiber angle versus distance from base to apex of the strip shown in (A), for two depths $z = 60 \mu\text{m}$ (dark grey squares) and $z = 160 \mu\text{m}$ (light grey circles). Error bars are expressed as standard deviation.

deformed when making histological sections. Note that DTI, which does not involve physical sectioning, gives results similar to that of our method. An attempt to minimize damage caused by histological sectioning was performed in rat RV by Young et al. (1998). They combined histological sectioning with confocal microscopy, by first imaging the bottom 60 μm of the block, then cutting the bottom 50 μm of tissue, and repeating this process until the entire block was imaged. Their qualitative results are similar to ours (see Figs. 5 and 7 in Young et al., 1998 and Figures 7A and 7B in this paper), and the total fiber rotation they measure (120°) is closer to our value (105.7°) than any other histological study. The relatively small difference (14°) may be attributed to the difference in species. Our preparations are not subjected to microtome sectioning since all sections are optical. This avoids the problems posed by mechanical distortion, alignment, and section loss of the specimen and enables us to image 2

mm of cleared ventricular tissue in an uninterrupted scanning session.

Although we can image as deep as 2 mm, it would be desirable to still image deeper within the tissue. Since the penetration depth is limited mostly by the residual scattering of the cleared tissue, the key to imaging deeper layers may lie in the use of near-infrared dyes (Matiukas et al., 2006, 2007), which have longer excitation and emission wavelengths so that the scattering within the tissue reduces. The dye di-4-ANBDQBS can be used in the near-infrared region provided that the photodetector is optimized for use in this region. In the future, we will take advantage of this property to further increase the penetration depth. Autofluorescence is a source of noise in our imaging method. We found that it occurs predominantly in blood clots; however, if heparin is administered before anesthetizing the animal, then the formation of blood clots could reliably be prevented. Regarding the accuracy of fiber direction,

we note that we are chemically treating the myocardium in a way that shrinks the tissue, and this, to some degree, distorts the fiber organization. The shrinkage we observe (10%) is, however, substantially less than that observed in both DTI and histology (15–35%, Kanai and Salama, 1995; Streeter et al., 1969).

In summary, the fiber mapping method we propose combines the strengths of DTI and histological methods; it allows for the mapping of fibers in a nondestructive manner (as DTI does) and it has spatial resolution of a few microns (as histological methods do). Our method avoids both the massive costs associated with using MRI scanners, and the time-consuming labor of preparing histological sections.

ACKNOWLEDGMENTS

We are grateful for the technical assistance of Zhen Li and Maochun Qin.

REFERENCES

- Abramoff MD, Magelhaes PJ, Ram SG. 2004. Image processing with ImageJ. *Biophotonics Int* 11:36–42.
- Arts T, Prinzen FW, Snoeckx LH, Rijcken JM, Reneman RS. 1994. Adaptation of cardiac structure by mechanical feedback in the environment of the cell: A model study. *Biophys J* 66:53–61.
- Baxter WT, Mironov SF, Zaitsev AV, Jalife J, Pertsov AM. 2001. Visualizing excitation waves inside cardiac muscle using transillumination. *Biophys J* 80:516–530.
- Burton RA, Plank G, Schneider JE, Grau V, Ahammer H, Keeling SL, Lee J, Smith NP, Gavaghan D, Trayanova N, Kohl P. 2006. Three-dimensional models of individual cardiac histoanatomy: Tools and challenges. *Ann N Y Acad Sci* 1080:301–319.
- Dodt HU, Leischner U, Schierloh A, Jahrling N, Mauch CP, Deininger K, Deussing JM, Eder M, Zieglgansberger W, Becker K. 2007. Ultramicroscopy: Three-dimensional visualization of neuronal networks in the whole mouse brain. *Nat Methods* 4:331–336.
- Fenton F, Karma A. 1998. Vortex dynamics in three-dimensional continuous myocardium with fiber rotation: Filament instability and fibrillation. *Chaos* 8:20–47.
- Helm PA, Tseng HJ, Younes L, McVeigh ER, Winslow RL. 2005. Ex vivo 3D diffusion tensor imaging and quantification of cardiac laminar structure. *Magn Reson Med* 54:850–859.
- Holmes AA, Scollan DF, Winslow RL. 2000. Direct histological validation of diffusion tensor MRI in formaldehyde-fixed myocardium. *Magn Reson Med* 44:157–161.
- Hort W. 1960. [Macroscopic and micrometric research on the myocardium of the left ventricle filled to varying degrees.]. *Virchows Arch Pathol Anat Physiol Klin Med* 333:523–564.
- Hsu EW, Muzikant AL, Matulevicius SA, Penland RC, Henriquez CS. 1998. Magnetic resonance myocardial fiber-orientation mapping with direct histological correlation. *Am J Physiol* 274:H1627–H1634.
- Jiang Y, Pandya K, Smithies O, Hsu EW. 2004. Three-dimensional diffusion tensor microscopy of fixed mouse hearts. *Magn Reson Med* 52:453–460.
- Jung BA, Kreher BW, Markl M, Hennig J. 2006. Visualization of tissue velocity data from cardiac wall motion measurements with myocardial fiber tracking: Principles and implications for cardiac fiber structures. *Eur J Cardiothorac Surg* 29 (Suppl 1):S158–S164.
- Kadish A, Shinnar M, Moore EN, Levine JH, Balke CW, Spear JF. 1988. Interaction of fiber orientation and direction of impulse propagation with anatomic barriers in anisotropic canine myocardium. *Circulation* 78:1478–1494.
- Kanai A, Salama G. 1995. Optical mapping reveals that repolarization spreads anisotropically and is guided by fiber orientation in guinea pig hearts. *Circ Res* 77:784–802.
- Karlon WJ, Covell JW, McCulloch AD, Hunter JJ, Omens JH. 1998. Automated measurement of myofiber disarray in transgenic mice with ventricular expression of ras. *Anat Rec* 252:612–625.
- Koide T, Narita T, Sumino S. 1982. Hypertrophic cardiomyopathy without asymmetric hypertrophy. *Br Heart J* 47:507–510.
- LeGrice IJ, Smail BH, Chai LZ, Edgar SG, Gavin JB, Hunter PJ. 1995a. Laminar structure of the heart: Ventricular myocyte arrangement and connective tissue architecture in the dog. *Am J Physiol* 269:H571–H582.
- LeGrice IJ, Takayama Y, Covell JW. 1995b. Transverse shear along myocardial cleavage planes provides a mechanism for normal systolic wall thickening. *Circ Res* 77:182–193.
- Lorensen WE, Cline HE. 1987. Marching cubes: A high resolution 3D surface construction algorithm. *Comput Graph* 21:163–169.
- Matiukas A, Mitrea BG, Pertsov AM, Wuskell JP, Wei MD, Watras J, Millard AC, Loew LM. 2006. New near-infrared optical probes of cardiac electrical activity. *Am J Physiol Heart Circ Physiol* 290:H2633–H2643.
- Matiukas A, Mitrea BG, Qin M, Pertsov AM, Shvedko AG, Warren MD, Zaitsev AV, Wuskell JP, Wei MD, Watras J, Loew LM. 2007. Near-infrared voltage-sensitive fluorescent dyes optimized for optical mapping in blood-perfused myocardium. *Heart Rhythm* 4:1441–1451.
- Miller CE, Thompson RP, Bigelow MR, Gittinger G, Trusk TC, Sedmera D. 2005. Confocal imaging of the embryonic heart: How deep? *Microsc Microanal* 11:216–223.
- Omens JH, May KD, McCulloch AD. 1991. Transmural distribution of three-dimensional strain in the isolated arrested canine left ventricle. *Am J Physiol* 261:H918–H928.
- Omens JH, MacKenna DA, McCulloch AD. 1993. Measurement of strain and analysis of stress in resting rat left ventricular myocardium. *J Biomech* 26:665–676.
- Panfilov AV, Keener JP. 1993. Generation of reentry in anisotropic myocardium. *J Cardiovasc Electrophysiol* 4:412–421.
- Punske BB, Taccardi B, Steadman B, Ershler PR, England A, Valencik ML, McDonald JA, Litwin SE. 2005. Effect of fiber orientation on propagation: Electrical mapping of genetically altered mouse hearts. *J Electrocardiol* 38:40–44.
- Roberts WC, Ferrans VJ. 1975. Pathologic anatomy of the cardiomyopathies. Idiopathic dilated and hypertrophic types, infiltrative types, and endomyocardial disease with and without eosinophilia. *Hum Pathol* 6:287–342.
- Sakhalkar HS, Dewhirst M, Oliver T, Cao Y, Oldham M. 2007. Functional imaging in bulk tissue specimens using optical emission tomography: Fluorescence preservation during optical clearing. *Phys Med Biol* 52:2035–2054.
- Scollan DF, Holmes A, Winslow R, Forder J. 1998. Histological validation of myocardial microstructure obtained from diffusion tensor magnetic resonance imaging. *Am J Physiol* 275:H2308–H2318.
- Scollan DF, Holmes A, Zhang J, Winslow RL. 2000. Reconstruction of cardiac ventricular geometry and fiber orientation using magnetic resonance imaging. *Ann Biomed Eng* 28:934–944.
- Streeter DD, Jr, Bassett DL. 1966. An engineering analysis of myocardial fiber orientation in pig's left ventricle in systole. *Anat Rec* 155:503–512.
- Streeter DD, Jr, Spotnitz HM, Patel DP, Ross J, Jr, Sonnenblick EH. 1969. Fiber orientation in the canine left ventricle during diastole and systole. *Circ Res* 24:339–347.
- Taccardi B, Lux RL, Ershler PR, MacLeod R, Dustman TJ, Ingebrigtsen N. 1997. Anatomical architecture and electrical activity of the heart. *Acta Cardiol* 52:91–105.
- Tezuka F, Hort W, Lange PE, Nurnberg JH. 1990. Muscle fiber orientation in the development and regression of right ventricular hypertrophy in pigs. *Acta Pathol Jpn* 40:402–407.
- Vetter FJ, McCulloch AD. 1998. Three-dimensional analysis of regional cardiac function: A model of rabbit ventricular anatomy. *Prog Biophys Mol Biol* 69:157–183.
- Vetter FJ, Simons SB, Mironov S, Hyatt CJ, Pertsov AM. 2005. Epicardial fiber organization in swine right ventricle and its impact on propagation. *Circ Res* 96:244–251.
- Waldman LK, Nosan D, Villarreal F, Covell JW. 1988. Relation between transmural deformation and local myofiber direction in canine left ventricle. *Circ Res* 63:550–562.
- Wickline SA, Verdonk ED, Wong AK, Shepard RK, Miller JG. 1992. Structural remodeling of human myocardial tissue after infarction. Quantification with ultrasonic backscatter. *Circulation* 85:259–268.
- Wu EX, Wu Y, Tang H, Wang J, Yang J, Ng MC, Yang ES, Chan CW, Zhu S, Lau CP, Tse HF. 2007. Study of myocardial fiber pathway using magnetic resonance diffusion tensor imaging. *Magn Reson Imaging* 25:1048–1057.
- Young AA, LeGrice IJ, Young MA, Smail BH. 1998. Extended confocal microscopy of myocardial laminae and collagen network. *J Microsc* 192:139–150.
- Zucker RM. 2006. Whole insect and mammalian embryo imaging with confocal microscopy: Morphology and apoptosis. *Cytometry A* 69:1143–1152.
- Zucker RM, Hunter S, Rogers JM. 1998. Confocal laser scanning microscopy of apoptosis in organogenesis-stage mouse embryos. *Cytometry* 33:348–354.